Overview of JT-60U Results Toward the Resolution of Key Physics and Engineering Issues in ITER and JT-60SA

A. Isayama for the JT-60 team
Japan Atomic Energy Agency, Naka, Ibaraki 311-0193, Japan
e-mail contact of main author: isayama.akihiko@jaea.go.jp

Abstract: This paper describes an overview of recent results in JT-60U since the last IAEA Fusion Energy Conference. Topics we particularly focus on are (1) mechanism determining the rotation profile and the effect of rotation on/from transport and stability, (2) edge localized mode (ELM) physics and active ELM control and (3) generation and accumulation of impurities. Analysis on the momentum transport has found that rotation with high pressure gradient can be reproduced by introducing the residual stress term proportional to the momentum diffusivity and the pressure gradient. Also, momentum diffusivity in an internal transport barrier (ITB) region is found to be reduced to a similar order of the ion thermal diffusivity. Comparison of the edge pedestal characteristics between JT-60U and JET with matched shape and operational parameters shows that the edge pressure does not change with increasing toroidal field ripple up to 1%, while linear decrease and increase in ELM frequency and rotation velocity, respectively, in the counter direction have been observed. Absolute evaluation of W accumulation in the core plasma by a spectroscopic method has clarified that W accumulation increases with increasing toroidal rotation in the counter direction while an H-mode was sustained even at W density of 10^{-3} of electron density. This experimental result on high W accumulation for counter rotation is found to be explained by (i) a newly introduced pinch effect which increases with increasing radial electric field strength and (ii) inward/outward pinch by radial electric field for co-/counter-rotation, respectively. Active control of neoclassical tearing mode (NTM) islands by electron cyclotron current drive has shown that the growth of NTM islands decelerates the plasma rotation. A transition to a low-rotation frequency state is found to occur for larger NTM islands. Statistical analysis of precursor of type I ELM shows small growth rate of $\gamma/\omega_A \sim 10^{-3}$. The precursor measured at different toroidal locations shows the toroidal mode number is 8–10 or 14–16. Analysis on the edge stability with inclusion of the rotation effect by using the MINERVA code has clarified that the edge stability is degraded with increasing difference between the eigenmode frequency and the toroidal rotation frequency, which is consistent with experimental observations. Energetic particle driven Wall Modes (EWMs) are found to trigger ELMs and decrease the ELM amplitude to half of that without EWM. Enhancement of ELM frequency by electron cyclotron heating in the edge region of the high-field side has been observed, and the frequency increase is 4 times larger compared with neutral beam injection cases with the same absorption power. Integrated simulation on pellet-triggered ELM with the TOPICS-IB code has clarified that the energy absorption by pellet and its further displacement due to $E \times B$ drift, as well as transport enhancement by the pellet, can trigger the ELM. Measurement of carbon dust generation with Mie scattering has found that dust distribution has a peak in far scrape-off layer, and penetration into the core plasma is not significant. Depth profile measurement of D and C in W-coated tiles (W thickness: 50 μm) has clarified that the ratio of D to C is 0.06±0.02 over 20 μm depth, suggesting D trapping by C in the W layer. Furthermore, new records on (i) beam energy of negative-ion-based NB (507 keV at 1 A) and (ii) output power of 110 GHz electron cyclotron waves (1.5 MW for 4 s from 1 gyrotron) have been achieved, which ensure and extend the heating and current drive capability in ITER and JT-60SA.

1. Introduction

Experiments in JT-60U completed with great success in August 2008 [1]. Even after the conclusion, physics and engineering research toward JT-60SA and ITER has been ceaselessly continued particularly focusing on resolving key issues for ensuing successful operations in these devices. In this paper, results in JT-60U are described. Key research topics are (1) mechanism determining the rotation profile and the effect of rotation on/from transport and stability, (2) ELM physics and active ELM control and (3) generation and accumulation of impurities. In particular, in these two years, understanding of experimental results through theoretical analysis and simulations has been progressed in many research areas. Much progress in inter-machine comparison has also been made as described later in this paper.

In addition to the physics research, development for performance enhancement of the heating/ current drive systems by negative-ion-based neutral beam (NNB) and electron cyclotron range

of frequency (ECRF) waves has been continued toward JT-60SA by using the JT-60 facilities. As described later in detail, new records on injection energy of NNB and injection power and pulse duration of ECRF have been achieved, which are promising for JT-60SA and ITER.

2. Rotation and Its Effect on/from Transport and Stability

In a tokamak plasma, profiles of pressure, current and rotation are complicatedly related one another, and the transport property and MHD stability of the plasma are determined by the resultant profiles. Thus, clarification of the basic properties of rotation and the influences of rotation on/from other physics parameters is a key physics issue.

2.1 Momentum transport in plasmas with large pressure gradient

Momentum transport in H-mode and internal transport barrier (ITB) plasmas has been investigated in detail [2] based on the same method used for momentum transport analysis, in which the momentum diffusion and convention are derived from torque modulation experiments. Contribution of the residual stress term to the intrinsic rotation in the momentum transport equation has been investigated. Rotation velocity profile with large pressure gradient (but not so large as ITB formation) is found to be reproduced by introducing a residual stress term, Π_{res}, proportional to the pressure gradient and momentum diffusivity, i.e., $\Pi_{res}=\alpha\chi_\phi\nabla p_i$. Here, α, χ_ϕ and ∇p_i are a constant, the momentum diffusivity and the ion pressure gradient, respectively. Figure 1(a) shows profiles of toroidal rotation velocity in an H-mode plasma with and without inclusion of the residual stress term. Rotation at ρ<~0.5, where pressure gradient is large, is well reproduced by this term. In addition, momentum diffusivity in a plasma with internal transport barrier (ITB) has been investigated. Profiles of the momentum diffusivity and ion thermal diffusivity with and without ITB are shown in Fig. 1(b)-(c). Reduction in the momentum diffusivity at the ITB region, ρ = 0.3-0.4, is observed, and the ratio of χ_ϕ to the ion thermal diffusivity, χ_ϕ/χ_i, is found to be in the order of unity while the convective term is almost unchanged.

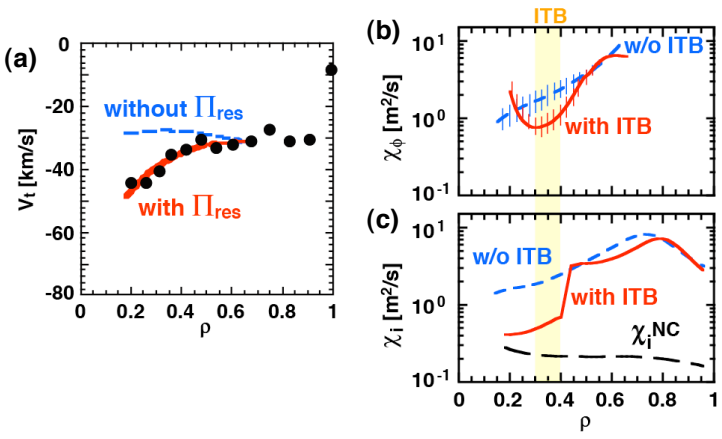

FIG. 1: (a) Toroidal rotation velocity profile. Closed circles are experimental data, and solid and broken lines are model-based profiles with and without the residual term, respectively. Profiles of (b) momentum diffusivity and (c) ion thermal diffusivity.

2.2 Comparative study on toroidal field ripple in JT-60U and JET

Toroidal field (TF) ripple is known to affect the fast-ion confinement. However, the effect of TF ripple on thermal energy confinement is not fully understood. In JT-60U and JET, inter-machine comparison on the TF ripple effect on the pedestal characteristics has been performed with the same plasma shape and operational parameters (JT-60U: I_p = 1.1 MA, B_t = 2.2-3.2 T; JET: I_p = 1.1 MA, B_t = 2.0 T) [3]. The range of the TF ripple rate, δ_R, is up to 1%, which is

comparable to ITER's TF ripple without ferritic steel tiles (the ripple rate is evaluated at the low-field side of the midplane). The edge toroidal rotation was found to decrease with increasing δ_R in both devices, as shown in Fig. 2(a). Note that the toroidal rotation in JT-60U becomes negative with increasing δ_R because fast-ion loss due to TF ripple induces counter rotation (Input torque is positive and similar in JT-60U and JET). On the other hand, no clear dependence was found for the edge pressure as shown in Fig 2(b). Electron pressure at the pedestal is almost unchanged at about 2.8 kPa when the pedestal density was scanned at 1-2.5 $\times 10^{19}$ m^{-3}. The dependence including its value was almost the same as in JT-60U and JET. In JT-60U, increase in f_{ELM} and decrease in ELM energy loss were observed with increasing δ_R.

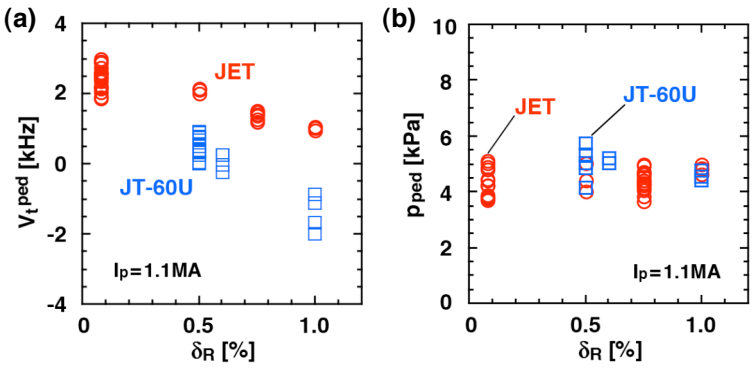

FIG. 2: TF ripple dependence of (a) toroidal rotation at the pedestal and (b) pedestal pressure.

2.3 Comparison of ITB characteristics in JT-60U and JET and rotation effect on ITB

The ITER advanced scenarios, Hybrid Scenario and Steady State scenario, utilize ITB for better plasma performance with high bootstrap current fraction. For better understanding of the formation and sustainment of ITB plasmas, comparative study of core transport properties of positive and negative shear plasmas with ITB in JT-60U and JET was performed by keeping the same plasma shape and toroidal field ripple [4]. In the experiments, under similar discharge scenarios, ITB was formed in both devices with similar profiles of ion temperature, electron temperature, normalized Larmor radius, normalized collision frequency, thermal beta and ratio of ion to electron temperatures etc. On the other hand, difference in the safety factor and density profile in the center (ρ<~0.3) was observed for strongly reversed shear plasmas; the central safety factor in JT-60U is very high due to the formation of current hole. In addition, electron density profile is more peaked and its value is larger for JT-60U. The effect of toroidal rotation, V_t, on ITB properties was also investigated in JT-60U by changing the combination of tangential neutral beams (NBs). Profiles in this scan are shown in Fig. 3. The rotation profile is shifted by this scan with almost keeping the shape as shown in Fig. 3(d). On the other hand, profiles of temperature, density and safety factor are almost unchanged and the

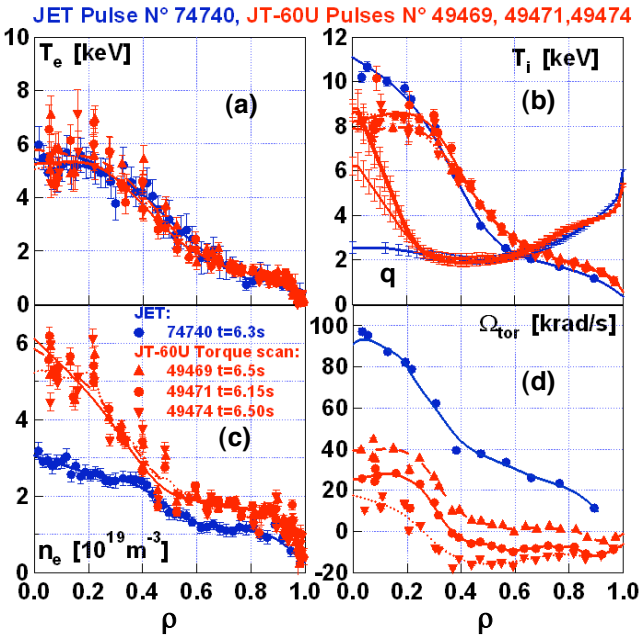

FIG. 3: Profiles for JT-60U/JET comparison of ITB. (a) electron temperature, (b) ion temperature and safety factor, (c) electron density, (d) toroidal rotation.

ITB structure is maintained in this range of scan.

2.4 Tungsten accumulation in rotating plasmas

Tungsten (W) is considered a promising material for the first wall due to its high melting temperature, low tritium retention and low sputtering yield. However, W is highly radiative and W accumulation in the core degrades the plasma performance. In JT-60U, a method for absolute calibration of the vacuum ultraviolet (VUV) spectrometer has been established, in which the VUV spectrum is compared with the visible light spectrum measured with the same sight line [5]. By this calibration, W content in the core plasma can be evaluated quantitatively. Figure 4 shows the dependence of (a) the ratio of W density to electron density and (b) radiative power from W on the toroidal rotation velocity at the center. The plasma is an H-mode plasma without ITB, and typical parameters are as follows: I_p = 1.5-1.6 MA, B_t = 3.2-3.9 T, q_{95} = 3.7-4.3 and NB power P_{NB} = 15 MW. W accumulation increases up to 0.1% with increasing V_t up to –150 km/s (The minis sign stands for counter-rotation). The radiation power obtained by this method is comparable to the increment of radiation power evaluated with bolometric measurement. A radiative collapse was observed for $n_W/n_e \sim 0.1\%$ and the radiation power of 2 MW. Electron temperature of about 4 keV inside ITB is considered to play a key role, and increase in W radiation and decrease in electron temperature successively occur because radiative power by W significantly increases below typically $T_e \sim 4$ keV. Actually, for a discharge with T_e higher than ~5 keV, an H-mode plasma was sustained even with $n_W/n_e \sim 10^{-3}$ (2-order higher than the acceptable W fraction in ITER), and radiative power by W was kept lower than 1 MW.

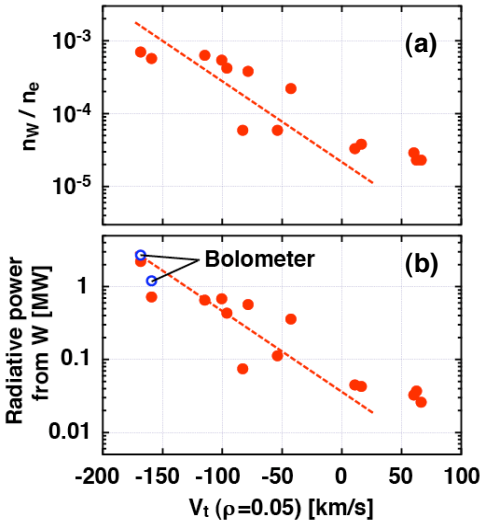

FIG. 4: Rotation dependence of (a) tungsten density normalized to electron density and (b) radiative power from tungsten.

Since W ions feel changes in electron temperature during their excursion on the drift orbit, their charge state can also change, and thereby their orbit is affected. As a result of analytical and numerical calculations, an inward pinch effect is found to arise due to the change in the charge state on the drift orbit of W [6]. The newly discovered inward pinch velocity is termed the pinch effect of high-Z impurities (PHZ). Figure 5(a) shows the dependence of the PHZ on the radial electric field evaluated by analytical calculation and simulation by the IMPGYRO code. The pinch velocity increases with the radial electric field, E_r, and it is nearly symmetrical with respect to the sign of E_r. Also, negative and positive radial electric fields by counter- and co-rotation cause inward and outward pinch of the high-Z impurity, respectively, under the

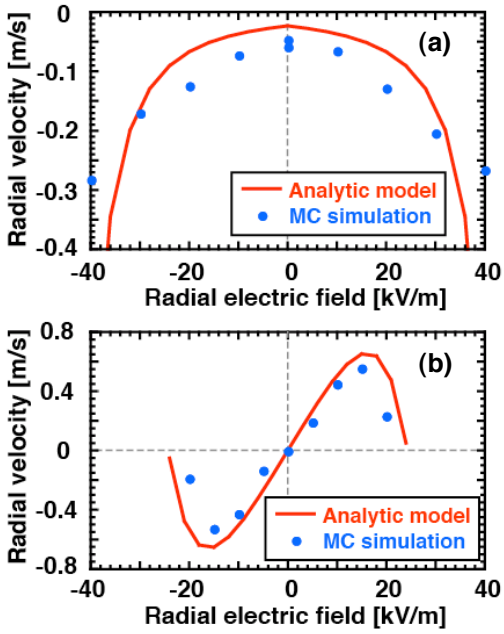

FIG. 5: (a) Dependence of PHZ on radial electric field and (b) dependence of pinch velocity due to plasma rotation on radial electric field.

influence of Coulomb collisions. As shown in Fig. 5(b), the dependence of the pinch velocity on E_r is antisymmetric with respect to E_r. As a result, the two effects enhance the inward pinch for negative E_r while they cancel each other for positive E_r. The results can explain JT-60U experimental results on larger tungsten accumulation for counter rotation.

2.5 Effect of NTM islands on rotation

Neoclassical tearing mode (NTM) has been observed in a high-beta plasma with a positive magnetic shear. Since the growth of magnetic islands associated with NTMs can interact with the surrounding conductive structure and decelerate the plasma rotation with its growth. In JT-60U, to investigate the deceleration effect experimentally, NTM island width was decreased and increased actively by aligned and misaligned electron cyclotron current drive (ECCD), respectively [7]. Figure 6(a) shows the dependence of the frequency of an $m/n=2/1$ NTM on magnetic perturbation amplitude. Here, m and n are the poloidal and toroidal mode numbers, respectively. The mode rotation frequency before ECCD in this discharge condition is 4 kHz, and it increases for mode stabilization and decreases for mode destabilization. Evolution of NTM islands in mode frequency–island width space is shown in Fig. 6(b). In this discharge, misaligned ECCD is applied at a low mode frequency. When the mode frequency reaches ~2.7 kHz, i.e., about half of the mode frequency at complete stabilization, the mode frequency suddenly decreases to 0.5 kHz. During this change, increase in the island width is less than 10%, suggesting that the change is a transition-like one. When the ECCD is turned off, the island width decreases and the mode frequency rapidly increases, showing again the transition-like behavior. It should be noted that the island with at the downward transition is larger than that at the upward transition. The existence of a hysteresis in the transition shows that once such transition occurs, NTM islands need to be reduced further to recover the rotation.

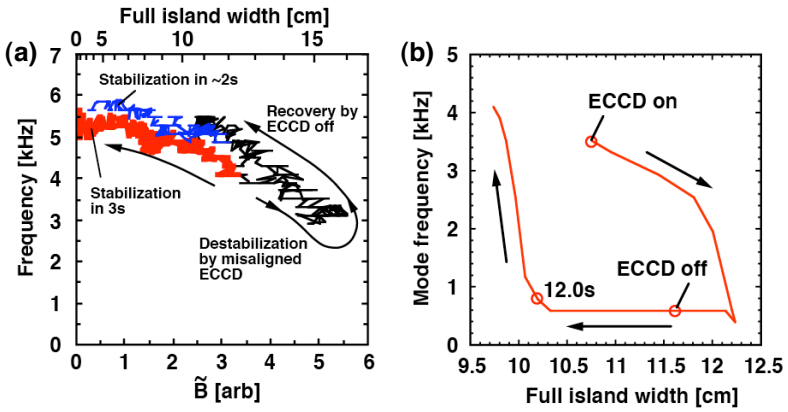

FIG. 6: Evolution of an m/n=2/1 NTM in the space of (a) mode frequency and magnetic perturbation amplitude and (b) mode frequency and full island width.

3. ELM Physics and Active ELM Control

An ELM, commonly observed in an H-mode plasma, causes transient heat load on divertor plates. The heat load can be intolerable for large-amplitude ELMs, particularly in ITER. Understanding the mechanism governing ELM stability and establishing methods for active ELM control without large degradation in confinement are thus important and urgent issues.

3.1 Characteristics of type I ELM precursor

Type I ELM is most commonly observed in experiments. In JT-60U, the process of ELM collapse was simultaneously measured by using diagnostics with high spatial and temporal resolutions [8]. Figure 7 shows an example of ELM precursor and a histogram of the growth

rate of the ELM precursor evaluated with a reflectometer. In this figure, discharges with different operational parameter, q = 3.6 and 4.5, p_{ped} = 9–20 kPa, are shown. The growth rate of 100–250 μs, which corresponds to $\gamma/\omega_A \sim 10^{-3}$, was found to be most frequently observed (γ and ω_A are the growth rate and the Alfvén angular frequency, respectively.). The result shows that the instability with such a small growth rate determines the onset condition of type I ELM. In addition, the toroidal mode number of ELM precursor was identified by evaluating the frequency of the precursor and the phase difference of the signals of the electron cyclotron emission diagnostics located 60° apart in the toroidal direction. The toroidal mode number is found to be 8–10 or 14–16. Stability analysis using the MARG2D code shows that the n=15 mode is unstable and the modes with n=12–14 and 16–17 are marginally unstable. These results suggest that the precursor corresponds to the linear growth phase of the peeling-ballooning modes.

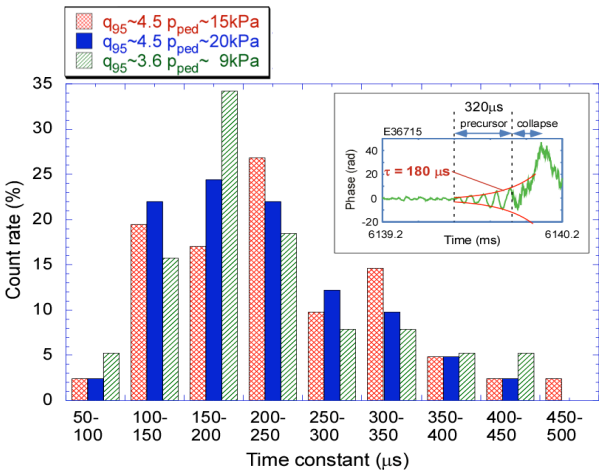

FIG. 7: Histogram of the growth rate of the precursor of type I ELM. An example of the evolution of the precursor is also shown in the window.

3.2 Effect of pressure gradient inside the pedestal top on ELM energy loss

Previous analysis using an integrated transport code TOPICS-IB, where the stability of type I ELM was calculated by a linear stability code MARG2D, showed that a steep pressure gradient inside the pedestal top enhances the ELM energy loss by broadening the eigenfunctions of unstable modes and thus extending the region of ELM-enhanced transport [9]. To verify the result, experiment data of high β_p discharges, relevant to the ITER Hybrid Scenario discharge, were analyzed [8]. Figure 8 shows the dependence of the loss fraction of stored energy by an ELM on the pressure gradient inside the top of the pedestal (R = 3.4 m, a = 0.9 m, I_p = 0.9 MA, B_t = 1.6 T, q_{95} = 3.3, net input power P_{net} = 6.5-9.4 MW, f_{ELM} =43-103 Hz). The value of the ELM-loss energy normalized to the pedestal stored energy, $\Delta W_{ELM}/W_{ped}$, increases with the pressure gradient inside the top of the pedestal normalized to that at the pedestal, p_{in}'/p_{ped}'. The magnitude of the dependence is also similar to the TOPICS-IB simulations. In the dataset, larger reduction rate of ion temperature ($\Delta T_i / T_i$) within the pedestal, as well as wider ELM-affected area, was found in a higher p_{in}'/p_{ped}' plasma. The value of the normalized collisionality, ν_{e*}, in the dataset is an order of 0.1, and no clear dependence of $\Delta W_{ELM}/W_{ped}$ on ν_{e*} was found, showing that the dependence of Fig. 8 is not attributed to the ν_{e*} dependence. The result shows that $\Delta W_{ELM}/W_{ped}$ is another important parameter determining the ELM energy loss, and that presently recognized data scattering is expected to be reduced by including this parameter, which will contribute to refining an ELM model.

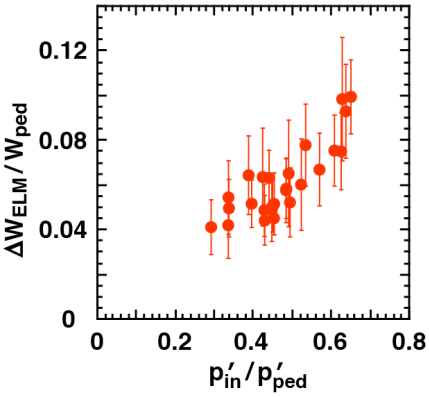

FIG. 8: Dependence of ELM energy loss normalized to the pedestal stored energy on the pressure gradient inside the pedestal normalized to that at the pedestal.

3.3 Effect of rotation shear on ELM stability

Behavior of type I ELM is known to be affected by toroidal rotation. Previous analysis by a linear MHD stability code, MINERVA, clarified that the edge stability related to type I ELM is degraded by increasing rotation shear [10]. To clarify the mechanism, potential energy including the rotation effect, δW_g, has been introduced. Then δW_g is decomposed into two terms, $\delta W_{g\text{-}eq}$ and $\delta W_{g\text{-}rot}$, which express the rotation effect on the equilibrium and that on the displacement, respectively [11]. Figure 9 (a) shows the growth rate of the peeling-ballooning mode with and without rotation. The growth rate with medium-n, which is thought to be related to type I ELM becomes larger by including the rotation effect. Dependence of δW_g , $\delta W_{g\text{-}eq}$ and $\delta W_{g\text{-}rot}$ on n is shown in Fig. 9(b). The $\delta W_{g\text{-}rot}$ term always act as a destabilizing term, and its magnitude increases with increasing n. The value of $\delta W_{g\text{-}rot}$ in Fig. 9(b) is nearly determined by a term relating to the difference between the eigenmode frequency and the equilibrium toroidal rotation frequency. Based on this theoretical analysis, stability of type I ELM in JT-60U experiments was analyzed. The fact that the edge rotation shear is stronger for counter-rotation than co-rotation is found to be the reason for lower stability of type I ELM, i.e, higher ELM frequency, in counter-rotating plasmas.

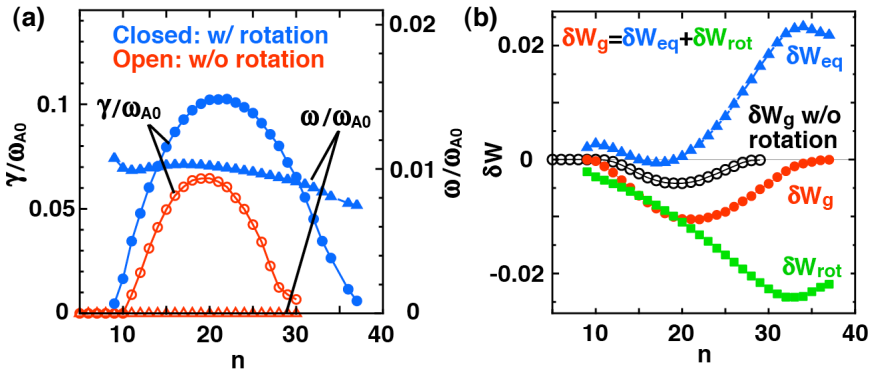

FIG. 9: (a) Dependence of the growth rate and mode frequency on the toroidal mode number, (b) Dependence of δW_g and its component on the toroidal mode number.

3.4 Effect of EWM on ELM

An bursting mode attributed to fast ions was previously observed in a high-beta regime above the ideal MHD limit without conducting wall ('no-wall limit'), and the mode was termed Energetic particle driven Wall Modes (EWMs) [12]. In an ELMy H-mode plasma with the beta value above the no-wall limit, EWM is found to induce ELM [13]. Figure 10 shows a typical

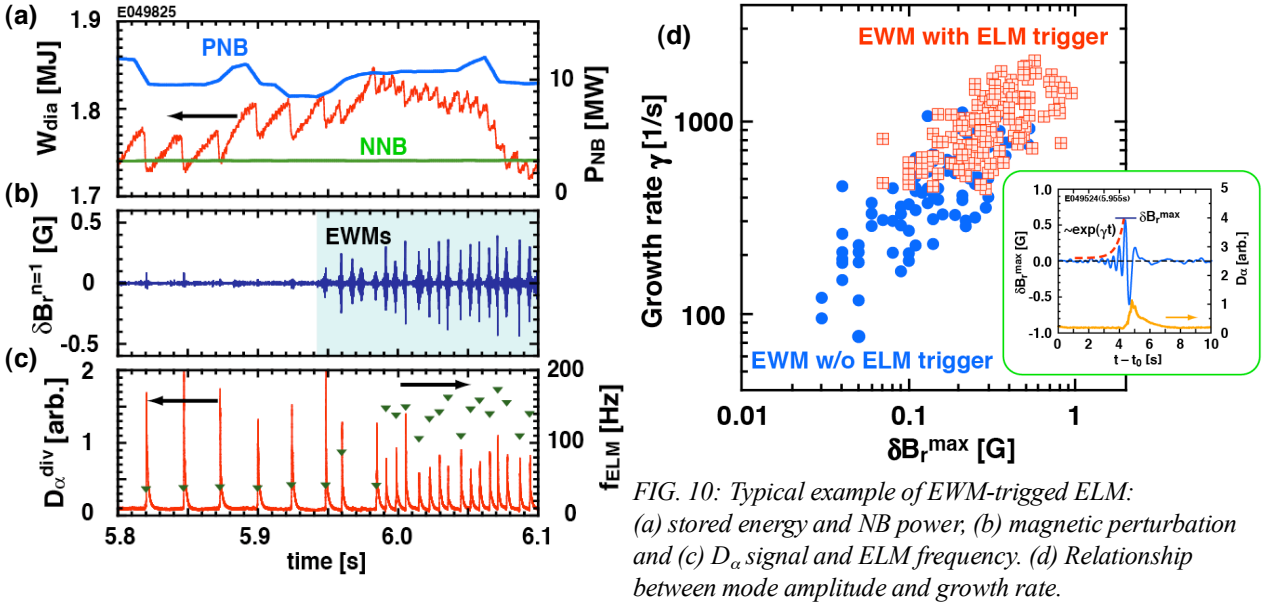

FIG. 10: Typical example of EWM-trigged ELM: (a) stored energy and NB power, (b) magnetic perturbation and (c) D_α signal and ELM frequency. (d) Relationship between mode amplitude and growth rate.

discharge where EWMs affect ELMs. After EWMs appear at $t = 5.94$ s, ELM is triggered by EWM, and the ELM frequency increases up to ~150 Hz, about 4 times higher than that before the EWM onset. At the same time, the ELM amplitude decrease to about a half with increasing ELM frequency. Decrement of stored energy due to each ELM is also reduced as shown in Fig. 10(a). In this series of discharges, EWMs do not always trigger ELMs. Figure 10(d) shows the relationship between the maximum mode amplitude, δB_r^{max}, and the mode growth rate, γ. The value of γ is evaluated by fitting the mode growth with the exponential function. The maximum mode amplitude is found to increase with the mode growth rate, and EWMs trigger ELMs only when the mode amplitude is large. Since the EWM amplitude is correlated with fast-ion fraction in the plasma and experiments suggest loss of fast ions by EWMs, the above result shows the importance of the fast-ion effect on ELM stability.

3.5 Effect of edge ECH on ELM behavior

Heating and current drive by electron cyclotron (EC) wave are advantageous because the deposition location can be highly localized, and the accurate control of the deposition location is feasible. In JT-60U, the effect of edge electron cyclotron heating (ECH) / ECCD on ELM has been investigated [8]. Figure 11(a) shows the temporal evolution of D_α emission, edge T_e, line-integrated n_e and stored energy. EC waves are deposited at the top corner of the high-field side as shown in Fig. 11(b). The ELM frequency doubles just after the edge EC wave injection for the absorption power of 1.6 MW. The increment of the ELM frequency is 4 times larger than that for NB injection of the same absorption power, as shown in Fig. 11(c). This shows the increment is not simply attributed to the increase in the input power. Together with the increase in the ELM frequency, reduction in $\Delta W_{ELM}/W_{ped}$ was observed. Such increase in f_{ELM} was observed only for EC wave injection to the top corner of the high-field side, and no clear change in f_{ELM} was observed for the injection to the edge of the low-field side. Fokker-Planck calculation shows that the ratio of the EC-driven current density to the total edge current density including the edge bootstrap current is about 1/16, and thus the effect of ECCD is not likely to be the reason for the frequency increase.

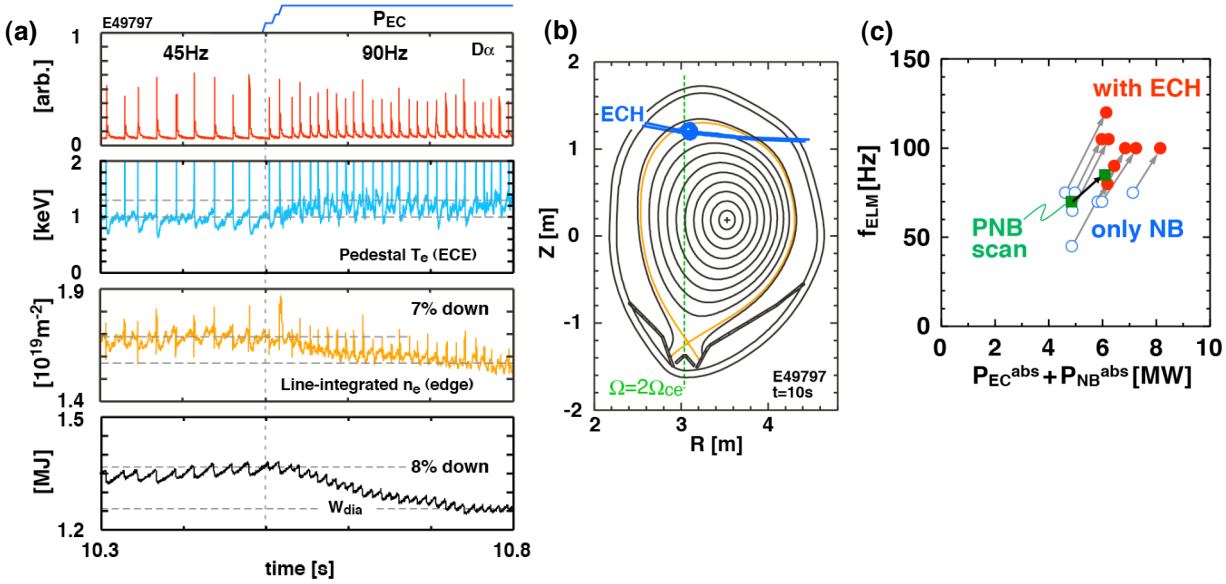

FIG. 11: (a) D_α intensity, edge electron temperature, line-integrated electron density and stored energy, (b) plasma cross-section and ray trajectory and (c) ELM frequency against absorption power.

3.6 Integrated simulation of pellet injection and ELM stability

Pellet injection is known to trigger an ELM and thus considered to be a tool for ELM pacing. To understand the mechanism of ELM triggering by pellet injection, integrated simulation of pellet-triggered ELM was carried out using the TOPICS-IB code, where the Ablated PeLlet with $E \times B$ drift (APLEX) model was implemented for evaluation of ablation, energy absorption, $E \times B$ drift and homogenization of injected pellets [14]. Two mechanisms for ELM onset have been found: (i) radial redistribution of background plasma pressure through the energy absorption by the pellet and subsequent penetration due to the $E \times B$ drift and (ii) transient enhancement of heat and particle transport caused by the sharp increase in local density and temperature gradients in the vicinity of ablated cloud, both of which cause steep pressure gradient, especially within the pedestal, contributing to ELM onset. TOPICS-IB simulation well reproduces the JT-60U experimental result of electron density profiles before and after the pellet injection. Also, integrated simulation on ELM stability analysis shows that the eigenfunction profiles become narrower for pellet-induced ELM due to destabilization of high-n modes, and that the ELM-induced loss becomes less than half of that without pellet injection.

4. Deposition, Penetration and Accumulation of carbon Impurities

In ITER and JT-60SA with high heat and particle flux at the divertor plate, (i) erosion and distribution of the divertor material and (ii) degradation of the plasma performance due to impurity accumulation in the plasma core are urgent issues. In addition, tritium inventory in the first wall is a primary concern in ITER.

4.1 Measurement of movement and profile of carbon dust

Carbon impurity eroded from the first wall is known to be accumulated as a form of dust. Since the penetration of carbon dust into the core plasma causes the degradation of the fuel purity, it is important to clarify the behavior of carbon dust. Radial distribution of carbon dust in the scrape-off layer (SOL) region was evaluated by measuring Mie scattering of YAG laser for Thomson scattering [15]. Figure 12 shows n_e and T_e profiles inside the separatrix and the event frequency of Mie scattering. Two of the profiles were obtained in discharges after disruptive discharges, in which carbon dust was redistributed over a wide area. The carbon intensity reaches the maximum in the far-SOL near the plasma facing component and quickly decreases toward the separatrix, showing that penetration of the carbon dust into the core plasma is not significant. In addition, mobility and lifetime of carbon dust have been measured by a fast camera with the frame rate of 2-6 kiloframes/s [15]. The direction of the dust movement is found to be the same as that of the plasma flow. Also, the fast dust speed was found to be about 1/100 of the SOL flow both in the main and divertor regions.

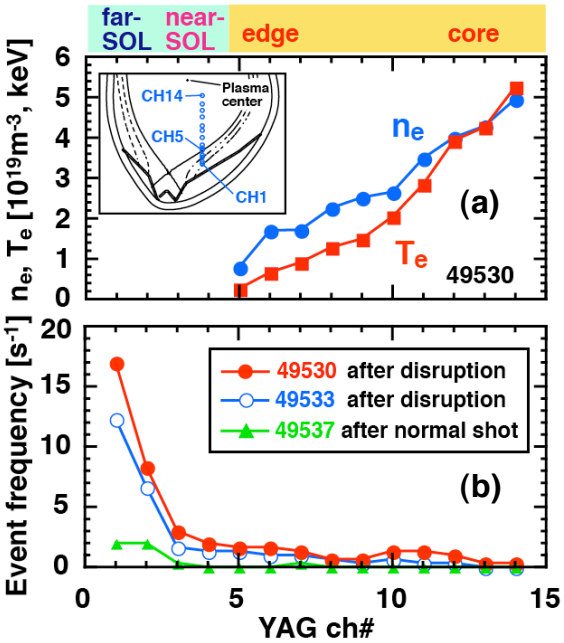

FIG. 12: (a) Profiles of electron density and electron temperature inside the separatrix and (b) event frequency of scattering by carbon dusts.

4.2 Measurement of D and C retention in W layer

In ITER, W coating is planned to be used at the first wall to reduce in-vessel tritium inventory. However, there is a possibility that carbon-based materials are used for high heat load components such as limiter. Clarification of the mechanism of the tritium retention in W coating is important for simultaneous use of W coating and carbon. Twelve W-coated CFC tiles with the W thickness of 50 μm, which cover ~5% of the toroidal length, was installed in the 2003-2004 campaign. Deuterium retention in W-coated CFC tiles exposed to JT-60U plasmas was investigated with surface analysis technique [16]. The amount ~10^{22} D/m^2 was found to be one order larger than that for W irradiated with similar fluence in laboratory experiments. Figure 13(a) shows the depth profile measured by Secondary Ion Mass Spectroscopy (SIMS). The ratio of D to C in the W coating was found to be uniform with 0.04-0.08 beyond ~5 μm in depth. Similar distribution of D and C suggests that D is trapped by C in the W layer, and D retention was increased by the C atoms. Figure 13(b) shows C concentration in the W layer measured by X-ray Photoelectron Spectroscopy (XPS). The C concentration after the tokamak plasma exposure was about 25% while the concentration before the exposure was a few percent. (The high carbon concentration at the surface of the tile without plasma exposure is attributed to the manufacturing process of the tiles and storage in air.) This shows that the dominant C source is implantation of eroded C from C tiles during plasma discharges.

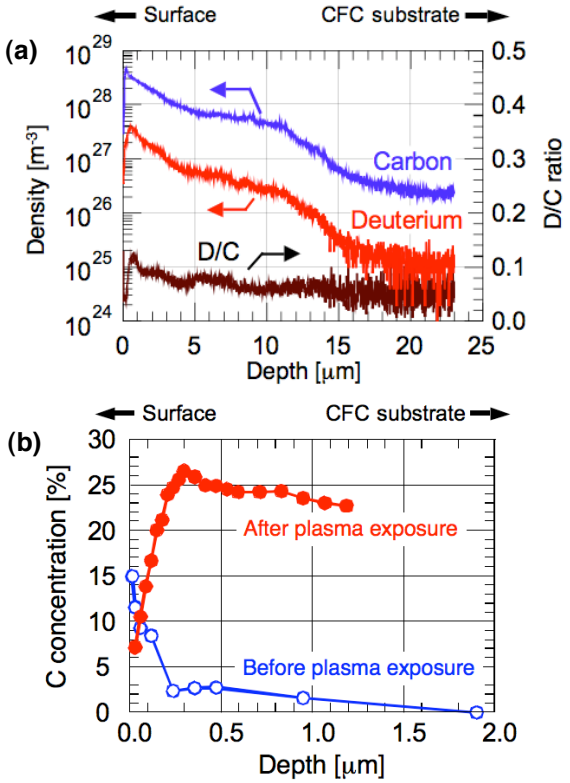

FIG. 13: Depth profile of (a) carbon and deuterium and (b) carbon concentration.

5. Performance Enhancement of Heating and Current Drive Systems

Capability of heating and current drive systems determines the performance of the plasma. NNBs are the main current driver both in ITER and JT-60SA and influence the non-inductive current drive fraction. EC waves significantly extends the potential of ITER and JT-60SA because they are used for many purposes such as preionization, localized electron heating, NTM stabilization and wall cleaning.

5.1 Extension of beam energy and beam current of NNB system

NNB for JT-60U is characterized by (a) 3-stage electrostatic acceleration up to 500 keV with 1.8-m diameter FRP (Fiber-Reinforced Plastic) rings and (b) multi-grids and multi-apertures (1080) on 5 segments. So far, the maximum beam energy of NNB for JT-60U was 416 keV, which was limited by electrical breakdown. The difficulty in achieving high voltage-holding capability comes form the fact that the mechanism of the voltage holding characteristics of large-area multi-aperture electrodes is unclear. To clarify the required gap length, the voltage holding capability was investigated by changing the gap length of the ion source. The minimum gap length was found to be a dominant factor for the voltage holding capability of the JT-60U

ion source. The ion sources for the NNB system was modified to allow higher voltage-holding capability by extending both the electrode-support distance and the electrode-electrode distance without causing large beam divergence and beam loss. As a result, the highest beam energy of 507 keV at 1 A and high beam current of 2.8 A at 486 keV have been achieved (Fig. 14) [17]. At the same time, voltage-holding capability of about 200 kV per single stage has been demonstrated, which is promising also for the 5-stage NNB system in ITER.

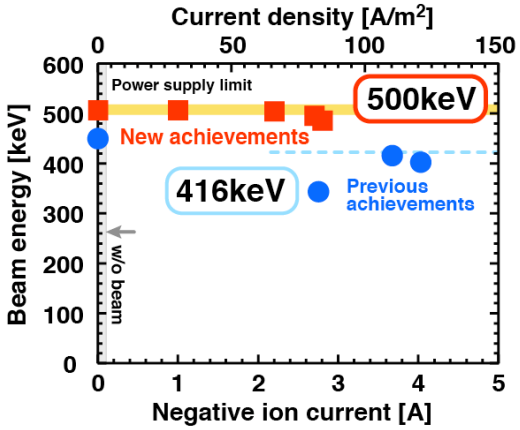

FIG. 14: Progress in the development of the NNB system.

5.2 Extension of output power and duration of ECRF system

Development of gyrotrons has been progressed toward high-power and long-pulse operation in JT-60SA, where 1 MW generation of 110 GHz EC wave per gyrotron with the pulse duration of 100 s is planned. To enhance the gyrotron capability, a new operational scenario has been developed. In the development, the following two operational regimes are chosen. One is the region where the startup of the desired mode, $TE_{22,6}$, is possible but long-duration sustainment is not allowed due to overload to the gyrotron. The other is the region where the oscillation of the $TE_{22,6}$ mode is not possible but longer-duration sustainment is possible from the viewpoint of the heat load. Operation using a gyrotron for JT-60U has found that startup and sustainment of the $TE_{22,6}$ mode can be realized by starting the oscillation from the former regime with larger voltage between the cathode and the anode and then quickly (~0.1 s) moving to the latter regime. As a result, the output power of 1.5 MW was achieved for 4 s [18], which is the world's highest power among output duration longer than ~1 s (Fig. 15). In addition, extension of the pulse width at 1 MW output has also been continued. By installing a new mode convertor, diffractive loss was reduced and temperature increase of the DC break, which was the major performance-limiting factor, reduced to about half. So far, 1 MW output for 30 s has been achieved.

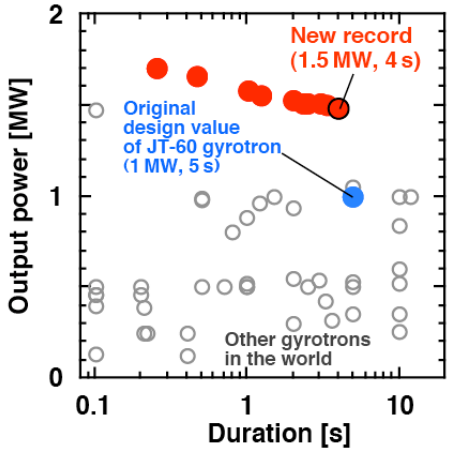

FIG. 15: Progress in gyrotron development.

6. Summary

Research and development have been continued in JT-60U toward successful operation in ITER and JT-60SA after its shutdown in 2008. In physics research, experiment analysis and theoretical analysis/simulation have been closely linked each other. Engineering development has also been performed using the JT-60 facilities. Topics we particularly focused on in these 2 years are (1) mechanism determining the rotation profile and the effect of rotation on transport and stability, (2) ELM physics and active ELM control, (3) generation and accumulation of impurities and (4) performance enhancement of heating and current drive systems. They are all urgent issues in ITER and JT-60SA. Major results are summarized as follows:

- Improvement in χ_ϕ inside ITB with a similar degree of χ_i has been observed. The residual stress term in the form of $\Pi_{res}=\alpha\chi_\phi\nabla p_i$ reproduces the toroidal rotation in a high-∇p region. Comparative study between JT-60U and JET has shown no clear change in the edge thermal pressure at the pedestal for TF ripple up to 1%, while linear change in the toroidal rotation. Also, ITB structure has been maintained under different toroidal rotations. Experimental observation of W accumulation for counter-rotating plasmas has been verified by analytical calculation and simulation through a newly introduced pinch effect. Rotation deceleration by the growth of NTM islands and transition of the mode frequency have been observed. And thus, different degrees of rotation effects on/from transport and stability have been clarified.
- Precursor of type I ELM with small growth rate of $\gamma/\omega_A\sim10^{-3}$ has been found to appear most frequently with n ranging 8–10 or 14–16. MINERVA code analysis has clarified the destabilizing effect of the rotation shear on the edge stability. Effects of EWM on ELM has been observed. Clarification on the mechanism of pellet-induced ELM by TOPICS-IB simulation and observation of increase in f_{ELM} by edge ECH are also shown. As these results suggest, while the initial phase of natural type I ELMs is considered to be determined by the peeling-ballooning limit, localized and/or transient disturbances and parameters inside and outside the pedestal have effects on the ELM stability.
- Measurement of carbon dust distribution has shown the largest amount on carbon dust in the far-SOL and small amount in the core plasma. Surface analysis has shown high D retention in W-coated tiles possibly due to D trapping by C accumulated in the W-coating. The results are considered to give an important guideline for the use of C tiles.
- New records have been achieved in the development of heating and current drive systems; the highest acceleration energy (507 keV) of the NNB system with the voltage-holding capability of ~200 keV per single stage; the highest output power (1.5 MW, 4 s) from a gyrotron of the ECRF system with the duration longer than ~1 s.

Acknowledgment

The JT-60 project is supported by a wide range of domestic and international collaborations. The authors would like to express their sincere gratitude to the contributors.

References

[1] OYAMA, N., et al., Nucl. Fusion **49** (2009) 104007.
[2] YOSHIDA, M., et al., this conference, IAEA-CN-180/EXC/3-2.
[3] URANO, H., et al., this conference, IAEA-CN-180/EXC/P8-17.
[4] LITAUDON, X., et al., this conference, IAEA-CN-180/EXC/P4-12.
[5] NAKANO, T., et al., submitted to J. Nucl. Material (2010).
[6] HOSHINO, K., et al., this conference, IAEA-CN-180/THC/P4-12
[7] ISAYAMA, A., et al., Plasma Fusion Res. **5** (2010) 037.
[8] OYAMA, N, et al., this conference, IAEA-CN-180/EXS/8-3.
[9] HAYASHI, N., et al., Nucl. Fusion **49** (2009) 095015.
[10] AIBA, N., et al., Nucl. Fusion **49** (2009) 065015.
[11] AIBA, N. et al., this conference, IAEA-CN-180/THS/P3-01.
[12] MATSUNAGA, G., et al., Phys. Rev. Lett. **103** (2009) 045001.
[13] MATSUNAGA, G., et al., this conference, IAEA-CN-180/EXS/5-3.
[14] HAYASHI, N., et al., this conference, IAEA-CN-180/THS/P3-02.
[15] ASAKURA, N., et al., this conference, IAEA-CN-180/EXD/P3-02.
[16] FUKUMOTO, M., et al., this conference, IAEA-CN-180/EXD/P3-10.
[17] KOJIMA, A., et al., this conference, IAEA-CN-180/FTP/1-1Ra.
[18] KOBAYASHI, T., et al., this conference, IAEA-CN-180/FTP/P6-13.

The JT-60 Team
N. Aiba, H. Akasaka, N. Akino, A. Ando[1)], T. Arai, N. Asakura, N. Ashikawa[2)], M. Baba[1)], J. Bialek[3)], A. Bierwage, S. Chiba, P. de Vries[4)], Y. Endoh[5)], H. Fujita[6)], T. Fujita, M. Fukumoto[7)], A. Fukuyama[8)], P. Gohil[9)], L. Grisham[10)], K. Hamamatsu, T. Hamano[11)], M. Hanada, K. Hasegawa, T. Hatae, R. Hatakeyama[1)], N. Hayashi, T. Hayashi, S. Higashijima, Y. Higashizono[12)], J. Hinata[5)], T. Hino[13)], S. Hiranai, Y. Hirano[14)], M. Hirota[15)], J. Hobirk[16)], A. Honda, M. Honda[15)], H. Horiike[6)], L. Horton[17)], Katsumichi Hoshino, Kazuo Hoshino[7)], N. Hosogane, J. Howard[18)], K. Iba[11)], H. Ichige, M. Ichimura[12)], K. Ida[2)], S. Ide, H. Idei[19)], Y. Idomura, K. Igarashi[5)], S. Iio[20)], Y. Ikeda, T. Imai[12)], S. Inagaki[19)], M. Inomoto[21)], A. Isayama, S. Ishida, Y. Ishige[5)], K. Ishii[1)], Y. Ishii, K. Itami, K. Itoh[2)], S. Itoh[19)], S. Jolliet[7)], S. Kado[21)], Y. Kagei[22)], Y. Kamada, I. Kamata[11)], A. Kaminaga, K. Kamiya, Y. Kashiwa, K. Kawahata[2)], M. Kawai, Y. Kawamata, H. Kawano[12)], H. Kawashima, H. Kawazome[23)], M. Kazawa, K. Kikuchi[5)], Y. Kishimoto[8)], S. Kitajima[1)], S. Kitamura, S. Kiuchi[5)], K. Kiyono, K. Kizu, T. Kobayashi[15)], T. Kohmoto[2)], Y. Koide, A. Kojima, M. Komata, T. Kominato[11)], K. Komuro[5)], M. Koubiti[24)], H. Kubo, N. Kubo[5)], K. Kurihara, G. Kurita, M. Lesur[25)], X. Litaudon[26)], T. Luce[9)], T. Maekawa[8)], K. Masaki, T. Masuda[21)], S. Masuzaki[2)], M. Matsukawa, T. Matsumoto, G. Matsunaga, Y. Matsuzawa[5)], T. Minami[2)], N. Miya, A. Miyamoto[11)], N. Miyato, Y. Miyo, T. Mizuuchi[8)], K. Mogaki, D. Moreau[27)], M. Mori, S. Moriyama, K. Nagasaki[8)], O. Naito, Y. Nakamura, T. Nakano, Y. Nakashima[12)], M. Nakatsuka[6)], K. Narihara[2)], G. Navratil[3)], S. Nemoto[5)], H. Nishimura[6)], T. Nishiyama, H. Numata[11)], Y. Ogawa[21)], Y. Ohmori, N. Ohno[28)], K. Ohshima[5)], K. Ohya[29)], M. Ohzeki[5)], A. Oikawa, F. Okano, J. Okano, M. Osakabe[2)], T. Oshima, N. Oyama, T. Ozeki, V. Parail[30)], A. Pigarov[31)], H. Saeki[11)], G. Saibene[32)], S. Sakakibara[2)], Y. Sakamoto, A. Sakasai, S. Sakata, T. Sakuma[11)], S. Sakurai, A. Salmi[33)], T. Sasajima, S. Sasaki, M. Sasao[1)], F. Sato[5)], Masayasu Sato, Minoru Sato, Y. Sato[5)], M. Sawahata, M. Seimiya, M. Seki, N. Seki[5)], Y. Shibama, K. Shibata[5)], Y. Shibata[28)], M. Shibayama[5)], K. Shimada, Katsuhiro Shimizu, Koichi Shimizu[5)], T. Shimizu [5)], M. Shimono, K. Shinohara, J. Shiraishi[15)], M. Sueoka, T. Sugimura[34)], A. Sukegawa, H. Sunaoshi, Hiroaki Suzuki[5)], Hiroshi Suzuki[11)], Masanobu Suzuki[11)], Mitsuhiro Suzuki[11)], S. Suzuki, Takahiro Suzuki, Takashi Suzuki[5)], Y. Takase[21)], M. Takechi, H, Takenaga, T. Takizuka, N. Tamura[2)], Hirohiko Tanaka[28)], Hitoshi Tanaka[8)], K. Tanaka[2)], Yasunori Tanaka[35)], Yutaka Tanaka[7)], K. Tanimoto[6)], M. Terakado, T. Terakado, K. Tobita, K. Toi[2)], H. Tojo[7)], S. Tokuda, T. Totsuka, K. Tsuchiya, Y. Tsukahara, M. Uchida[8)], Y. Ueda[6)], K. Uehara, Y. Uesugi[35)], H. Urano, L. Urso[16)], K. Ushigusa, K. Usui, Kazuhiko Wada[5)], Kenji Wada[5)], K. Watanabe[2)], S. Wiesen[36)], M. Yagi, J. Yagyu, I. Yamada[2)], K. Yamauchi, K. Yamazaki[28)], T. Yamaguchi[34)], K. Yokokura, H. Yoshida[6)], M. Yoshida, Z. Yoshida[21)], A. Yoshikawa[37)], M. Yoshinuma[2)], H. Zohm[16)], H. Zushi[19)]

Japan Atomic Energy Agency
1) Tohoku University, Japan
2) National Institute for Fusion Science, Japan
3) Columbia University, USA
4) FOM institute Rijnhuizen, Netherlands
5) Fixed-term Engineer
6) Osaka University, Japan
7) Post-Doctoral Fellow
8) Kyoto University, Japan
9) General Atomics, USA
10) Princeton Plasma Physics Laboratory, USA
11) Collaborating Engineer
12) University of Tsukuba, Japan
13) Hokkaido University, Japan
14) Nihon University, Japan
15) Senior Post-Doctoral Fellow
16) Max-Planck-Institut für Plasmaphysik, Germany
17) EFDA-CSU Culham, Culham Science Centre, UK
18) Australian National University, Australia
19) Kyushu University, Japan
20) Tokyo Institute of Technology, Japan
21) The University of Tokyo, Japan
22) Research Organization for Information Science & Technology, Japan
23) Kagawa national College of Technology, Japan
24) Universite de Provence, France
25) Ecole Polytecnique, France
26) CEA, IRFM, France
27) Association EURATOM-CEA, France
28) Nagoya University, Japan
29) Tokushima University, Japan
30) EURATOM/CCFE Fusion Association, UK
31) University of California, San Diego, USA
32) The European Joint Undertaking for ITER and the development of Fusion Energy
33) Aalto University, Finland
34) Seconded staff
35) Kanazawa University, Japan
36) EURATOM/FZJ Association, Germany
37) Shizuoka University, Japan